The G305 star forming complex: Wide-Area molecular mapping of NH$_3$ and H$_2$O masers

L.Hindson[1,2]⋆, M.A. Thompson[1], J.S. Urquhart[2], J.S. Clark[3], B. Davies[4,5]
[1]Centre for Astrophysics Research, Science and Technology Research Institute, University of Hertfordshire, College Lane, Hatfield, AL10 9AB, UK
[2] Australia Telescope National Facility, CSIRO Astronomy and Space Science, PO Box 76, Epping, NSW, 1710, Australia
[3]Department of Physics and Astronomy, The Open University, Walton Hall, Milton Keynes MK7 6AA
[4]Center for Imaging Science, Rochester Institute of Technology, 54 Lomb Memorial Drive, Rochester, NY 14623, USA
[5]School of Physics & Astronomy, University of Leeds, Woodhouse Lane, Leeds LS2 9JT

ABSTRACT

We present wide area radio (12 mm) Mopra Telescope observations of the complex and rich massive star forming region G305. Our goals are to determine the reservoir for star formation within G305 using NH$_3$ to trace the dense molecular content, and thus, the gas available to form stars; estimate physical parameters of detected NH$_3$ clumps (temperature, column density, mass etc); locate current areas of active star formation via the presence of H$_2$O and methanol masers and the distribution of YSOs and ultra compact HII regions associated with this region. This paper details the NH$_3$ (J,K), (1,1), (2,2) and (3,3) inversion transition and 22 GHz H$_2$O maser observations. We observed a ∼1.5° × 1° region with ∼ 2′ angular resolution and a sensitivity of ∼ 60 mK per 0.4 km s^{-1} channel. We identify 15 NH$_3$ (1,1), 12 NH$_3$ (2,2) and 6 NH$_3$ (3,3) clumps surrounding the central HII region. The sizes of the clumps vary between < 2.6 and 10.1 pc, the average kinetic temperature of the gas is 25 K. We calculate clump masses of > 10^4 M$_\odot$ and find the total molecular mass of the complex to be ∼ 6×10^5 M$_\odot$. We note the positions of 56 star formation tracers, and discover a high degree of correlation with detected NH$_3$ clumps. We have detected 16 H$_2$O masers, find they correlate with the detected ammonia clumps and in general are found closer to the NH$_3$ clump cores than star formation tracers of later evolutionary stages.

Key words: Ammonia – Molecular clouds – Massive Star Formation – Maser

1 INTRODUCTION

High mass stars (> 8 M$_\odot$) have a significant effect on their surrounding volume, injecting a large amount of energy into the natal cloud. This feedback energy takes the form of high velocity winds, outflows, expanding HII regions, high energy radiation and eventually supernovae. These processes have a profound effect, potentially triggering new star forming events (Elmegreen & Lada 1977; Habing & Israel 1979; Elmegreen 2002) or alternatively disrupting future formation by dispersing the natal cloud (Elmegreen & Lada 1977).

The G305 star forming region lies in the Scrutum Crux arm within the galactic plane at $l = 305°$, $b = 0°$. At a distance of ∼ 4 kpc and with an age of 3-5 Myr, the complex is one of the most luminous HII regions in the galaxy (Clark & Porter 2004), centred on the open clusters Danks 1 & 2 and the Wolf-Rayet star WR 48a. Numerous infrared hotspots, HII emission, ultra compact (UC) HII regions and molecular maser emission suggest that O type stars are currently forming, with a radio flux indicative of > 31 deeply

embedded 07V stars (Clark & Porter 2004). G305 provides an excellent laboratory in which to study massive star formation as it is one of the closest sites of massive star formation in the galaxy and contains multiple sites and different epochs of star formation over its large scale, allowing the investigation of evolution and environmental effects such as triggering.

In Fig. 1, we present a three colour composite image of G305, constructed using images obtained from the Galactic Legacy Infrared Mid-Plane Survey Extraordinaire (GLIMPSE) (Benjamin et al. 2003; Churchwell et al. 2009). The 8 μm filter is of particular interest as it is dominated by polycyclic aromatic hydrocarbon (PAH) features, these are excited in the surface layers of molecular clouds that are exposed to a significant amount of UV radiation and therefore an excellent tracer of photo-dominated regions (PDRs) (Leger & Puget 1984). For this reason PDRs are a good signpost for molecular regions that are undergoing a strong interaction with a nearby HII region (Urquhart et al. 2003). In this image we show the positions of Danks 1 & 2 and WR 48a which are believed to be the driving force behind the central diffuse HII region (Clark & Porter 2004).

Here we report on our first observations of NH$_3$ (1,1), (2,2),

---

⋆ E-mail: l.hindson@herts.ac.uk
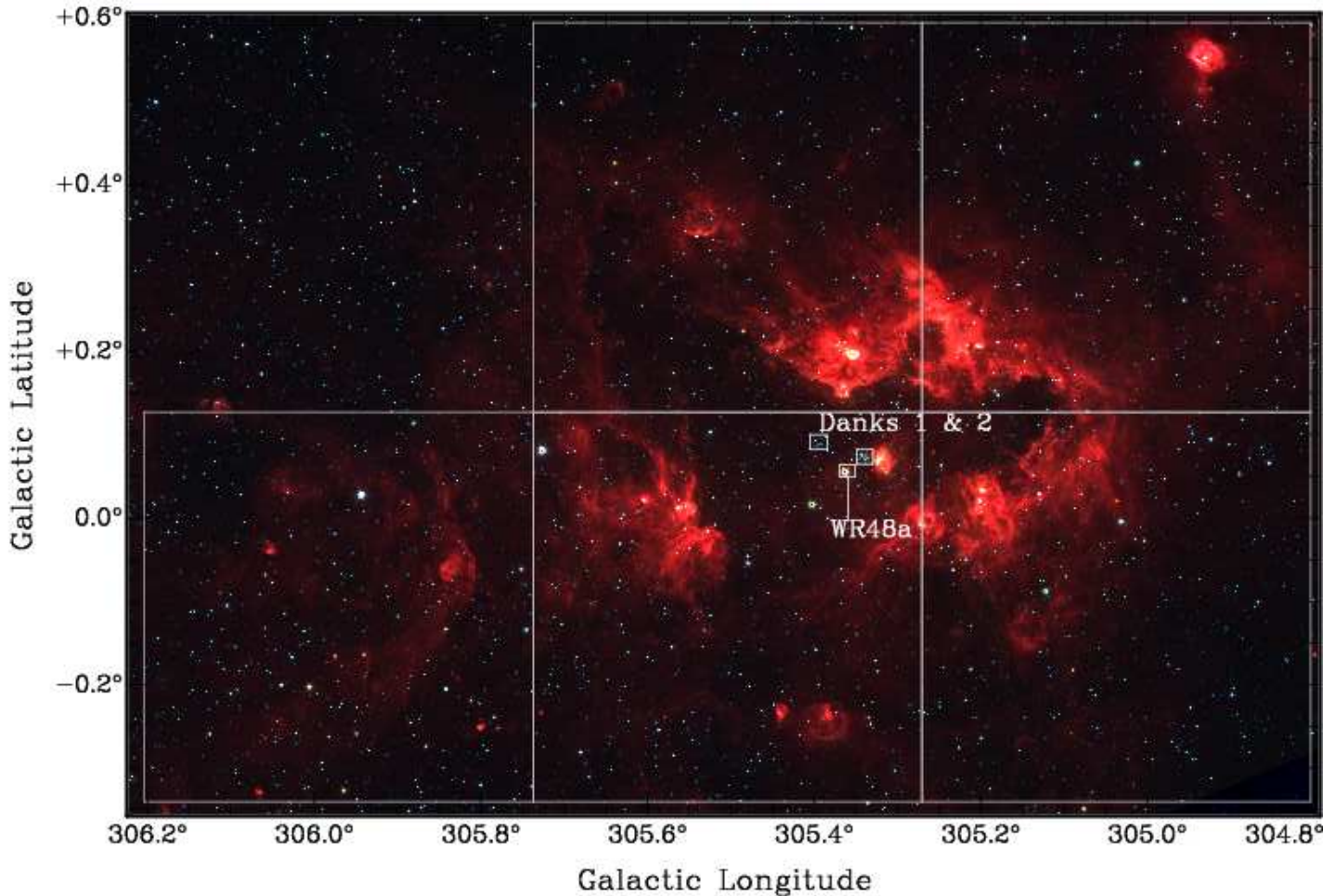
Figure 1. Wide-field 3 colour image (8 μm (red), 4.5 μm (green) and 3.6 μm (blue)) GLIMPSE image of the G305 complex, with the positions of Danks 1 & 2 over-plotted with boxes. Our scan area is shown by light grey boxes.

(3,3) and the 22 GHz H_2O maser line, using the Mopra radio telescope. Previous imaging of G305 by the H_2O Southern Galactic Plane Survey (HOPS) (Walsh et al. 2008) has revealed the presence of NH_3 hotspots in G305, but lacked the depth to trace less massive clumps and moderate column densities. Using NH_3 which has an effective critical density of $10^4 - 10^5$ cm^{-3} (Ho & Townes 1983), we are able to trace the dense gas structure of the region. Surveys of such dense regions are critical to relating the properties of the molecular gas to the star-forming properties of the cloud. We intend to make use of these low resolution NH_3 maps as a pathfinder for future high resolution interferometric observations. We also report the positions of 22 GHz H_2O maser emission, which have been shown to be good tracers of the early stages of low and high mass star formation (Furuya 2003). In high mass YSOs, H_2O masers have been found to be associated with hot molecular cores, molecular outflows and jets. H_2O maser emission is believed to highlight an evolutionary phase before the onset of a UC HII region around an embedded star (Furuya 2003). In low mass YSOs, H_2O masers are found to be associated with predominantly class 0 YSOs and in excited shocks of protostellar jets in the vicinity of the star. Thus, they are an excellent signpost of the early stages of star formation.

In Section 2 we present details of the observations and the data reduction processes, in Section 3 we present our observational re-

sults and derive basic parameters, Section 4 presents our discussion and in Section 5 we present a summary of our results.

2   OBSERVATIONS & DATA REDUCTION PROCEDURES

Observations were made using the Australia Telescope National Facility (ATNF) telescope Mopra. This is a 22m antenna located 26km outside the town of Coonabarrabran in New South Wales at an elevation of 866 meters above sea level and at a latitude of 31 degrees south.

The telescope is equipped with a 12 mm receiver with a frequency range of 16 to 27.5 GHz. The UNSW Mopra spectrometer (MOPS) is made up of four 2.2 GHz bands which overlap slightly to provide 8 GHz continuous bandwidth. The Mopra spectrometer has two possible modes, narrow and broadband modes. The narrow band or "zoom" mode of MOPS was used and allowed us to observe 16 spectra simultaneously, with a bandwidth of 137.5 MHz over 4096 channels in each zoom window. This gives a channel spacing of 34 kHz, corresponding to a velocity resolution of ~ 0.4 km s^{-1} at 24 GHz. We set our zoom windows to match those used in the HOPS survey, see Table 1 in Walsh et al. (2008) for details of targeted lines. Our line detections are summarised in Table 1. In this paper we focus upon the analysis of the NH_3 and H_2O maser

Table 1. Lines detected, central frequency and the size of the Mopra beam at the given frequency.

Line	Freq (GHz)	HPBW (″)
H_2O (6-5)	22.235	144
NH_3 (1,1)	23.694	136
NH_3 (2,2)	23.722	136
NH_3 (3,3)	23.870	136
HC_3N (3,2)	27.294	120
$H69\alpha$	19.951	164
CH_3OH ($3_2 - 3_1$)	24.928	131
CH_3OH ($4_2 - 4_1$)	24.933	131
CH_3OH ($2_2 - 2_1$)	24.934	131
CH_3OH ($6_2 - 6_1$)	24.959	131
CH_3OH ($7_2 - 7_1$)	25.018	131

detections. We postpone the analysis of the remaining detections ($H69\alpha$, CH_3OH and HC_3N) to future publications combining this data with forthcoming observations of the cm-wave radio continuum (Hindson et al 2010, in prep) and multi-line studies of CH_3OH and HC_3N.

In order to cover the 1.5×1 degree scale of G305 and remain within scan length constraints, our observations consisted of $5 \times 28' \times 28'$ maps with a $3'$ overlap between adjacent maps (see Fig. 1). All maps were obtained using the fly mapping mode, in which the telescope scans along the sky taking spectra at regular intervals along lines of constant latitude and longitude. The maps were sampled with $51''$ spacing to give Nyquist sampling at the highest frequency of 27.4 GHz and better than Nyquist at lower frequencies. The fastest scan rate of 2s per point was used, an off source position was observed periodically to remove sky emission. Combined with the limited scan speed and large map size a single map took ~ 2 hours to complete in one scan direction, and 4 hours with two orthogonal (Galactic latitude & longitude) co added scans, used to reduce striping. We obtained 5 complete co added scans of each of the 5 regions, taking a total of 50 hours of observing time collected over a number of nights in April and May of 2009. The weather conditions were changeable over this period with water vapour levels between 15 and 25 mm and system temperatures of ~ 100 K, with a variation in T_{sys} of no more than 20% during the course of any particular map. During times of dense cloud cover and rain, observations were halted as these conditions caused system temperatures of well over 120 K.

The data were reduced using the packages LIVEDATA and GRIDZILLA, both are AIPS++ packages written by Mark Calabretta[1] for the Parkes radio telescope and adapted for Mopra. LIVEDATA performs a bandpass calibration for each row using the off-source data followed by fitting user specified polynomial to the spectral baseline. GRIDZILLA calculates the pixel value from the spectral values and weights using the weighted mean estimation. We use a Gaussian smoothing kernel of $2'$ with a cut off radius of $0.5'$. This produces a map with minimal smoothing giving a pixel size of $0.5' \times 0.5'$ and a sensitivity of ~ 60 mK per 0.4 km s^{-1} channel, approximately twice as deep as the ongoing HOPS survey (Walsh et al. 2008). We make use of a recent study into the efficiency of Mopra (Urquhart et al. 2010) to convert the NH_3 antenna temperatures into main beam temperatures using the efficiency at 23 GHz of 0.64.

3 RESULTS AND ANALYSIS

In this section, we describe the distribution of NH_3 clumps as well as the locations of detected H_2O masers in the G305 complex. We define individual NH_3 clumps using the clump finding algorithm FELLWALKER and present their source averaged spectra. We derive the basic physical properties of the detected clumps from their NH_3 emission.

3.1 The distribution of ammonia clumps and H₂O masers

In Fig. 2, we present peak temperature contour plots of NH_3 (1,1) and (2,2) emission, the noise in the map is ~ 0.06 K. We show the location of H_2O maser emission detected towards G305 (blue crosses). The ammonia contours are overlaid onto a grayscale GLIMPSE 5.4 μm image, which also shows PAH emission highlighting the PDR. We use the 5.4 μm image because it is not as bright as the 8 μm band and so avoids the problem of saturation commonly encountered with the 8 μm band. We detect a number of NH_3 clumps in four distinct regions around the central HII region. Using WR 48a as a reference, we define the four regions of emission as (Galactic) north east (NE), north west (NW), south east (SE) and west (W). Within these regions, we distinguish 15 NH_3 (1,1), 12 NH_3 (2,2) clumps and 6 NH_3 (3,3) clumps. The majority of clumps are located around the periphery of the central cavity, with the higher transitions located mainly towards the PDR boundary. We detect 16 H_2O masers distributed throughout the region, all but two are found to be within the bounds of NH_3 emission. Of the 14 masers associated with NH_3 emission, eleven are found close to the clump cores, no NH_3 core is associated with more than one maser detection. Weak NH_3 clumps (excluding clump 11) in the western region appear to be devoid of H_2O maser emission. Detected clumps have been defined and numbered according to the output generated by the clump finding algorithm FELLWALKER (see section 3.1.1) and H_2O masers are numbered according to Table 5.

NW Region: Within this region we detect three NH_3 (1,1) clumps and one NH_3 (2,2) and (3,3) clump centred within clump 4. We detect three H_2O masers in this region within the boundaries of clump 4 and 7, these are close to but offset from the peak emission of the ammonia clumps. Ammonia clumps are connected by a surrounding region of low emission in the (1,1) transition and clump 4 appears to be elongated in the direction away from the central exciting stars. Unlike the other clumps in the complex, the emission peak in clump 4 is coincident with strong 5.4 μm emission towards the centre, indicating that the direction of the powerful (possibly ionising) radiation is impacting from our perspective, face on with the cloud, this area of strong PAH emission is also coincident with a HII (see Clark & Porter (2004) Fig. 2).

NE Region: This region contains two NH_3 clumps positioned behind one another, with clump 1 positioned further to the north, both clumps exhibit NH_3 (1,1), (2,2) and (3,3) emission. We detect two H_2O masers in this region both are located near the cores of the detected clumps but again they are slightly offset from the NH_3 peak. Clump 1 is host to the strongest peak and average main beam temperatures in the complex in both NH_3 (1,1), (2,2) and (3,3) emission lines (1.21, 0.66 and 0.42 K respectively) and it is the largest single clump detected (10.1 pc). The clumps are bounded by a region of low emission and are separated by a region of lower density. The two clumps are offset from what

Figure 2. Contour map of the peak temperature NH_3 (1,1) and (2,2) emission towards G305 in black and red contours respectively. Emission is over-plotted onto a GLIMPSE 5.4 μm (greyscale) image, detected H_2O masers are shown by blue crosses and numbered according to Table 5. Contours begin at 0.15 K and increment by 0.1 K, the noise in the map is 0.06 K. The clump numbers are shown for reference within circles and clump areas are shown as light grey outlines. Following our nomenclature we separate the complex into four regions of emission with grey boxes.
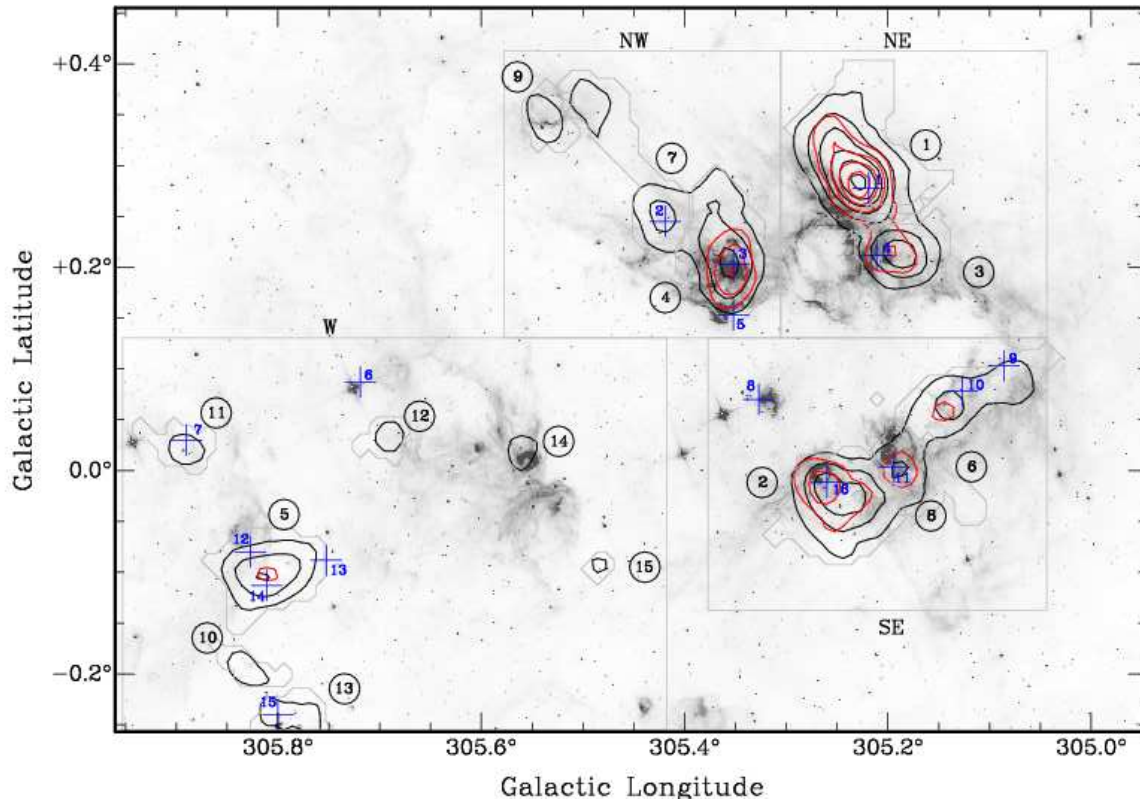
appears to be a bubble of intense PAH emission to the west that is also coincident with a HII region (see Clark & Porter (2004) Fig. 2).

SE Region: NH_3 (1,1) emission is observed in an unbroken strip parallel to the PDR and central cavity boundary, we observe three separate clumps within this strip, all of which are coincident with NH_3 (1,1) and (2,2) emission at the clump centres with NH_3 (3,3) detected within clump 2 and 8. We detect four water masers all within the bounds of the NH_3 (1,1) emission, three of these masers are found in close proximity to the detected ammonia clump peaks. Clump 2 appears to be extended in the direction away from the central clusters. We also note two strong PAH features on the periphery of clump 2 and in the region separating clump 8 and 6 on the inward side of the ammonia emission with the region between clump 8 and 6 also being the location of a HII region.

W Region: The region to the west of WR 48a shows a different morphology to previous regions. Here we find 7 isolated clumps of weak emission extending away from the centre of G305 as opposed to large clumps. The strongest NH_3 (1,1) source and the only source of visible NH_3 (2,2) and (3,3) emission are located some distance from the boundary PDR in clump 5. Six H_2O masers were detected, five of which are in close proximity to NH_3 clumps. We note that the PDR in this region appears to be dispersed to the north and south leaving only a small area of PAH emission coincident with clump 14.

3.1.1 Fellwalker *Clumpfind*

We have chosen to use the STARLINK tool CUPID [2] to automatically detect clumps in our 2D map, in particular the Fellwalker algorithm developed by David Berry (Berry et al. 2007). The Fellwalker algorithm works by finding the paths of steepest gradient from each pixel in the image. Starting with the first pixel in the image each of the surrounding pixels are inspected to locate the pixel with the highest ascending gradient, this process continues until a peak is located (i.e. a pixel surrounded by flat or descending gradients). The pixels along this path are assigned an arbitrary integer to represent their connection along a path. All pixels in the image are inspected in a similar process and the image is segmented into clumps by grouping together all paths that lead to the same peak value. The pixels belonging to paths that lead to a single peak are then defined as belonging to that particular clump. For a fuller description of this process see Berry et al. (2007). The Fellwalker algorithm is best used on images that have had the background subtracted, this has been performed using the background tracing and subtraction algorithm Findback in the CUPID package to subtract the uniform background of 0.06 K from the peak temperature, moment integrated image. The parameters of the detected NH_3 (1,1), (2,2) and (3,3) clumps can be found in Tables 2, 3 and 4. Fellwaker is not a widely used clump finding algorithm and so we carried out a number of checks using better known algorithms such as

GAUSSCLUMPS and CLUMPFIND to check for consistency, as well as performing manual aperture photometry checks. The FELL-WALKER algorithm gives very similar results to GAUSSCLUMPS, CLUMPFIND and manual aperture photometry with a significantly higher robustness to varying input parameters (see e.g. Pineda et al. 2009, for a discussion of the effect of varying the step size in CLUMPFIND). Due to the simplicity and robustness of FELL-WALKER we chose to use this algorithm to segment our images into clumps and extract the photometry for each clump.

3.2 NH₃ clump spectra

In Fig. 3, we present source averaged NH_3 (1,1) and (2,2) spectra for each clump region defined by FELLWALKER (shown as a grey outline surrounding the contours in Fig.2). In Fig. 4, we present the NH_3 (3,3) spectra averaged over the (3,3) emission region. All spectra have been Hanning smoothed to improve the noise to ~ 0.01 K per ~ 0.8 km s^{-1} channel. We have applied the same NH_3 (1,1) clump area results to the NH_3 (2,2) emission, therefore the (1,1) and (2,2) clump spectra are averaged over the same area, this allows us to make comparisons between the transitions. We should only expect to see seven strong detections in the NH_3 (2,2) and even fewer in the (3,3) transition that are coincident with NH_3 (1,1) emission, as seen in the peak temperature contour map Fig. 2. This is not the case, Fig. 3 clearly shows faint NH_3 (2,2) emission in twelve clumps and we see 6 NH_3 (3,3) detections in Fig. 4, this is due to the improved signal to noise from applying Hanning smoothing. We note the velocity of the NH_3 (2,2) and (3,3) emission appears at approximately the same velocity as the NH_3 (1,1) emission in all cases, for the particularly weak NH_3 (2,2) and (3,3) emission this provide supporting evidence that it is indeed real. The NH_3 (3,3) emission area is much smaller in geometric size than the (1,1) emission, therefore averaging the (3,3) spectra over the (1,1) area significantly lowers the temperature of the (3,3) emission due to beam dilution. We make use of NH_3 (3,3) emission to highlight areas of higher temperature and for this reason we have created NH_3 (3,3) source averaged spectra shown in Fig. 4 in order to better highlight the warmer clumps.

The hyperfine nature of the NH_3 (1,1) inversion transition provides a good indicator of optical depth through the ratio of intensity between the main and satellite lines. For this reason we have applied hyperfine fitting to all the NH_3 (1,1) spectra. Due to insufficient signal to noise, we are unable to resolve hyperfine structure in the NH_3 (2,2) emission and so we have applied Gaussian fitting. We only fit a Gaussian to the NH_3 (2,2) and (3,3) data if we can be confident that it is a true detection and the peak emission is $> 3\sigma$, thus only clumps 10, 11 and 15 are left with no (2,2).

Profiles were fitted using the IDL functions CURVEFIT for NH_3 (1,1) and GAUSSFIT for the NH_3 (2,2) and (3,3) lines. The model line profiles are over plotted in red in Fig. 3 and 4. The GAUSSFIT function computes a non-linear least-squares fit to the data. The CURVEFIT function uses a gradient-expansion algorithm to compute a non-linear least squares fit to a user-supplied function with an arbitrary number of parameters. Iterations are performed until the chi square changes by a specified amount, or until a maximum number of iterations have been performed. To fit the ammonia profiles we assume all the components have equal excitation temperatures and that the ammonia line widths and separations are identical to laboratory values.

We find line widths range from 1.7 km s^{-1} to 10.0 km s^{-1}. The thermal part of the line width accounts for only 0.28 km s^{-1} (for $T_{kin} = 30$ K) we therefore assume the line widths are largely dom-

inated by non-thermal turbulent motion. It can be clearly seen that several spectra exhibit blended main line and first satellite lines, this may be caused by emission from several unresolved clumps with differing velocities. The NH_3 (3,3) line widths are found to be wider than the lower transition counterparts for all clumps with the exception of clump 5.

3.3 H₂O masers

Sixteen H_2O masers were detected towards G305, their positions, velocity (LSR), velocity range and peak flux can be found in Table 5. It is important to note that due to the large size of the Mopra beam ($\sim 2'$), we are currently unable to determine the location of the emission to better than a few 10s of arcseconds. However follow up observations currently being obtained by the HOPS survey (Walsh et al. 2008) will accurately determine the locations to within a few arc-seconds. We make use of a recent study into the efficiency of Mopra by Urquhart et al (submitted 2010), specifically Table 3, to convert H_2O maser antenna temperatures to Jy using the conversion factor of 12.4. We find 6 new H_2O masers in the region, Walsh et al. (2008) show a detection of two H_2O maser at $l = 305.55$, $b = -0.02$ and $l = 305.85$, $b = +0.07$ which we did not detect. The only apparent explanation for this is H_2O maser variability, since our observational setup mimicked the HOPS survey and we obtained deeper, less noisy maps we should expect to detect all of the H_2O masers reported in Walsh et al. (2008) and more. Future HOPS observations should clarify this ambiguity. H_2O maser emission was detected across a broad velocity range between -120.8 and -10.4 km s^{-1} with a peak intensity varying between 2.4 and 1087.8 Jy, these values are characteristic of H_2O maser emission (Breen et al. 2007). The peak V_{LSR} and velocity range match well with the velocity of the NH_3 emission, it is clear that all detected H_2O masers are associated with G305 with the exception of maser 12, which has a peak velocity of -97.6 km s^{-1} and a velocity range that does not coincide with the G305 complex.

3.4 Analysis

In the following section, we present a standard analysis of the ammonia clumps using the spectra shown in Fig. 3.

3.4.1 Optical depth

Using the hyperfine structure, we extract the optical depth from the ratio of satellite to main line intensity, using Eq. (1) from Ho & Townes (1983):

$$\frac{\triangle T_\alpha^*(J, K, m)}{\triangle T_\alpha^*(J, K, s)} = \frac{1 - e^{-\tau(J,K,m)}}{1 - e^{-\alpha\tau(J,K,m)}} \qquad (1)$$

where $T_\alpha^*(J, K, m)$ is the observed antenna brightness temperature, (m,s) refer to the main and satellite hyperfine components, $\tau(J, K, m)$ is the optical depth of the main component and α is the ratio of intensity for the satellite compared to the main component [a = 0.28 and 0.22 for the (1,1) satellites]. An implicit assumption is that the beam filling factors are equal as are the excitation temperatures for the different hyperfine components. This is a reasonable assumption because of the very close energy separations and the small probability of special excitation mechanisms that differentiate between the hyperfine components (Ho & Townes 1983).
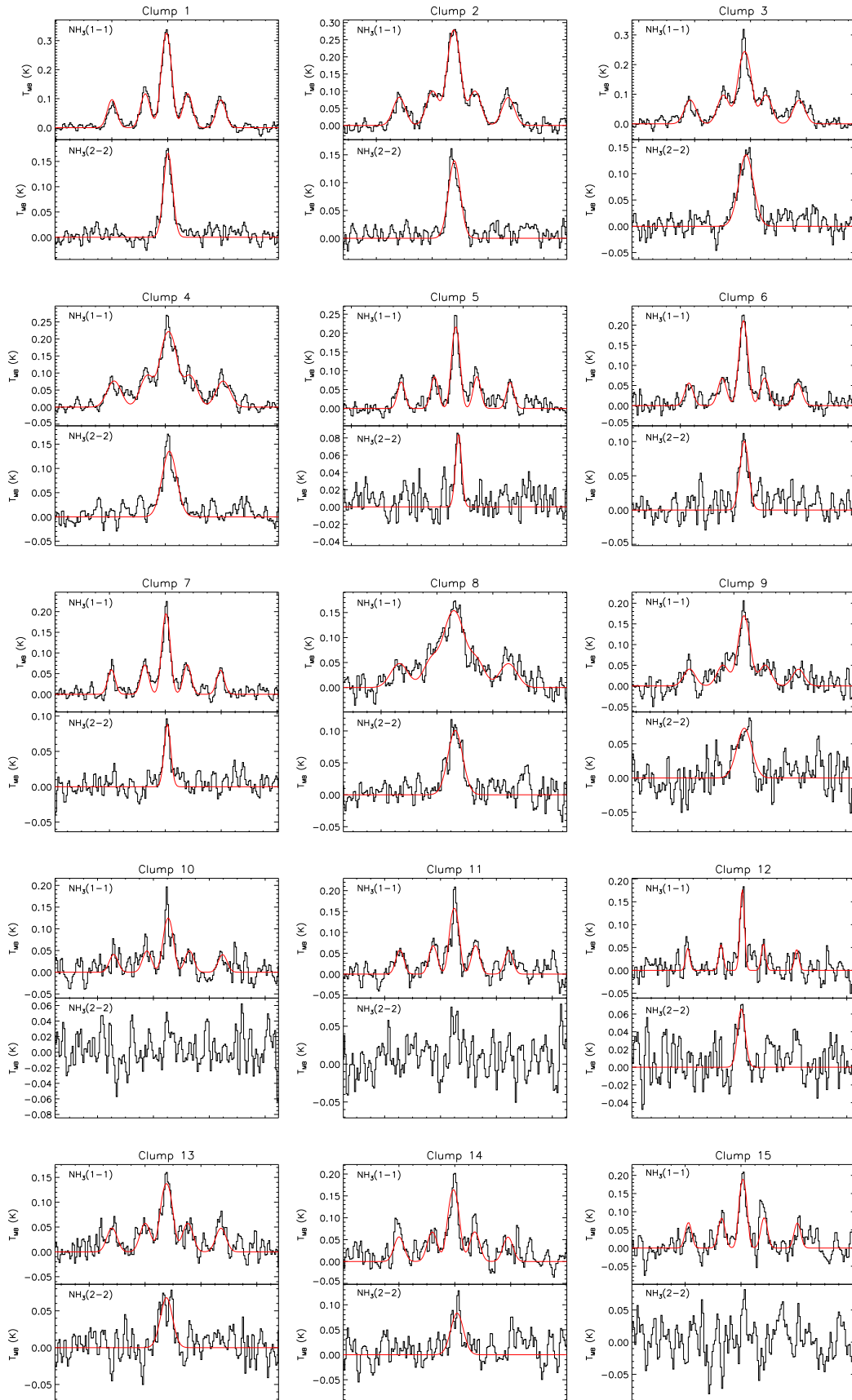
Figure 3. Clump averaged spectra of the 15 NH$_3$ clumps towards G305. Clumps have been integrated spatially over the clump area defined by Fellwalker and Hanning smoothed to provide a sensitivity of ~ 0.01 K per ~ 0.8 km s^{-1} channel. Hyperfine fitting is applied to the (1,1) emission and Gaussian fitting to the (2,2), shown as red overplots.

Table 2. NH$_3$ (1,1) clump properties, showing central position, velocity, diameter (geometric average), peak main beam temperature and clump averaged main beam temperature. We can only resolve clump diameters of > 2.6 pc at 4 kpc with the Mopra beam. These values are taken from the spectra averaged over the NH$_3$ (1,1) clump region defined by Fɛʟʟᴡᴀʟᴋᴇʀ

Region	Clump No	Peak		V_{LSR}	FWHM ΔV	Diameter	Peak $T_{MB}(1,1)$	Avg $T_{MB}(1,1)$
		Galactic (l)	Galactic (b)	(km s^{-1})	(km s^{-1})	(pc)	(K)	(K)
NE	1	305.23	0.29	-40.4	3.8	10.1	1.21	0.33
	3	305.19	0.21	-42.1	4.6	5.2	0.56	0.22
NW	4	305.36	0.20	-38.8	5.6	7.6	0.55	0.22
	7	305.42	0.25	-39.8	3.1	7.4	0.46	0.19
	9	305.54	0.34	-36.4	4.8	3.4	0.32	0.17
SE	2	305.26	-0.02	-32.3	4.9	7.3	0.74	0.28
	8	305.19	0.01	-34.0	7.1	5.2	0.43	0.15
	6	305.14	0.061	-37.4	3.4	7.0	0.45	0.21
W	5	305.82	-0.11	-42.7	3.0	6.0	0.60	0.22
	10	305.83	-0.19	-34.7	3.5	3.2	0.28	0.12
	11	305.89	0.02	-35.1	3.2	3.9	0.27	0.16
	12	305.69	0.04	-37.4	1.7	2.9	0.34	0.18
	13	305.77	-0.25	-32.3	4.1	3.9	0.34	0.14
	14	305.56	0.02	-40.4	3.9	3.8	0.34	0.16
	15	305.48	-0.10	-39.3	2.6	2.9	0.31	0.19

Table 3. NH$_3$ (2,2) clump properties, showing central position, velocity, diameter (geometric average), peak main beam temperature and clump averaged main beam temperature, these values are taken from the spectra averaged over the NH$_3$ (1,1) clump region defined by Fɛʟʟᴡᴀʟᴋᴇʀ .

Region	Clump No	Peak		V_{LSR}	FWHM ΔV	Diameter	Peak $T_{MB}(2,2)$	Avg $T_{MB}(2,2)$
		Galactic (l)	Galactic (b)	(km s^{-1})	(km s^{-1})	(pc)	(K)	(K)
NE	1	305.23	0.28	-39.9	3.8	6.3	0.66	0.17
	3	305.20	0.21	-41.6	6.2	4.3	0.32	0.14
NW	4	305.36	0.19	-38.6	6.2	4.5	0.34	0.14
	7	305.42	0.25	-39.2	2.9	< 2.6	0.39	0.09
	9	305.49	0.35	-36.3	6.3	< 2.6	0.30	0.07
SE	2	305.26	-0.02	-32.1	5.0	5.2	0.46	0.14
	8	305.19	0.00	-33.5	6.3	3.0	0.31	0.10
	6	305.15	0.03	-37.1	3.7	< 2.6	0.45	0.10
W	5	305.84	-0.07	-41.7	2.5	2.6	0.33	0.08
	12	305.69	0.06	-37.7	3.2	< 2.6	0.23	0.07
	13	305.89	-0.25	-32.3	5.1	< 2.6	0.25	0.07
	14	305.57	0.028	-39.2	4.4	< 2.6	0.26	0.08

3.4.2 Excitation Temperature

Once the optical depth of the NH$_3$ line is known the excitation temperature T_{ex} of the NH$_3$ (1,1) inversion can be derived using Eq. 2 in Ho & Townes (1983):

$$T_B(\nu) = T_0 \left(\frac{1}{e^{T_0/T_{ex}} - 1} - \frac{1}{e^{T_0/2.7} - 1} \right) (1 - e^{(-\tau\nu)}) \qquad (2)$$

where $T_0 = h\nu/k$, T_{MB} is the main beam telescope brightness temperature and T_{ex} is the source excitation temperature. We assume a background temperature of 2.7 K. This approach yields very low excitation temperatures $T_{ex} \sim 3$ K for a beam filling factor of 1, which is a result of beam dilution and smoothing due to the large Mopra beam. This low value of T_{ex} introduces significant error due to being so close to the background temperature and leads to lower limits for the mass of the detected clumps. We therefore assume a more representative excitation temperature of $T_{ex} = 10$ K for the rest of our analysis (Harju et al. 1993). We can make an estimate of the excitation by assuming a beam filling factor, it is likely that the beam filling factor is < 10%, for a beam filling factor of 0.1 we find the average excitation temperature to be $\sim$ 7.4 K, close to our assumed value of $T_{ex} = 10$ K.

3.4.3 Column Density

The column density, N_u, of the molecules in the upper state of the transition $u \rightarrow l$ can be expressed as a function of the integrated optical depth of the line using Eq. (3) from Harju et al. (1993):

$$N_u = \frac{3h\epsilon_0}{2\pi^2} \frac{1}{|\mu_{ul}|^2} F(T_{ex}) \int \tau \Delta V \qquad (3)$$

where $|\mu_{ul}|$ is the transition dipole moment (in Cm) and the function $F_{T_{ex}}$ is defined by:

$$F(T_{ex}) = \frac{1}{e^{T_0/T_{ex}} - 1} \qquad (4)$$

where $T_0 = h\nu_0/k$, the integration of τ is with respect to velocity. The application of the formula above depends on whether we have been able to determine τ, e.g., from a hyperfine fit as in the case of the (1,1) transition.

$$\int \tau \, dv = \frac{\sqrt{\pi}}{2\sqrt{ln2}} \Delta V \tau_0 \qquad (5)$$

where ΔV is the FWHM of the line profile. For the inversion transitions of NH$_3$(J, K) the squares of the transition dipole moments can be written as:

Table 4. NH$_3$ (3,3) clump properties, showing central position, velocity, diameter (geometric average), peak main beam temperature and clump averaged main beam temperature. Clump values are derived from the NH$_3$ (3,3) source averaged spectra Gaussian fit

Region	Clump No	Peak		V$_{LSR}$	FWHM ΔV	Diameter	Peak T$_{MB}$(3,3)	Avg T$_{MB}$(3,3)
		Galactic (l)	Galactic (b)	(km s^{-1})	(km s^{-1})	(pc)	(K)	(K)
NE	1	305.22	0.28	-40.2	4.8	5.7	0.42	0.20
	3	305.20	0.21	-42.0	7.6	3.8	0.36	0.20
NW	4	305.35	0.20	-38.6	7.1	4.9	0.36	0.20
SE	2	305.25	-0.02	-32.2	5.9	4.4	0.42	0.15
	8	305.19	0.00	-33.6	10.0	3.4	0.23	0.08
W	5	305.81	-0.1	-41.9	1.4	< 2.6	0.28	0.14
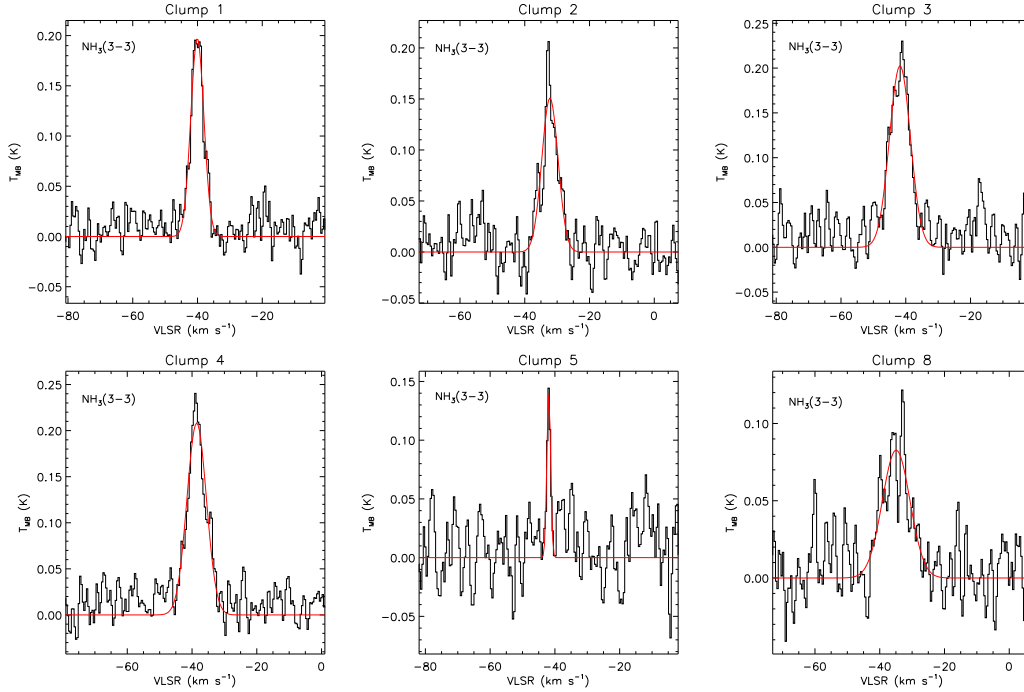
Figure 4. Source averaged spectra of the 6 NH$_3$ (3,3) clumps towards G305. Clumps have been integrated spatially over the NH$_3$ (3,3) emission area, spectra have been Hanning smoothed to provide a sensitivity of ~ 0.01 K per ~ 0.8 km s^{-1} channel. Gaussian fitting is applied, shown as red overplots.

Table 5. H$_2$O maser positions, peak velocity, velocity range and peak flux. Asterisks above the maser number show new detections over those identified by Walsh et al (2008). Previously detected H$_2$O masers are detailed in Table 2 in Walsh et al (2008)

Region	Maser Number	Peak		V$_{LSR}$ Peak	Velocity Range	Peak Flux
		Galactic (l)	Galactic (b)	(km s^{-1})	(km s^{-1})	(Jy)
NE	1*	305.22	0.28	-34.0	-37.7, -33.1	8.5
	4	305.21	0.21	-36.8	-44.5, -15.9	248.0
NW	2*	305.41	0.25	-32.1	-76.3, -32.2	2.4
	3	305.35	0.20	-30.9	-87.6, -18.1	64.1
	5	305.35	0.15	-32.7	-39.9, -20.4	294.0
SE	8	305.33	0.07	-42.7	-61.3, -26.8	217.8
	9*	305.09	0.1	-48.6	-50.1, -46.6	4.8
	10	305.13	0.08	-35.9	-34.9, -34.5	6.1
	11	305.20	0.00	-36.3	-36.8, -24.5	12.1
	16	305.26	-0.1	-23.1	-22.0, -22.5,	3.6
W	6	305.72	0.09	-39.9	-41.8, -38.6	8.5
	7	305.89	0.03	-24.5	-36.8, -22.2	43.6
	12*	305.83	-0.08	-97.6	-120.8, -85.4	13.3
	13*	305.75	-0.08	-45.8	-45.4, -43.6	7.2
	14*	305.81	-0.11	-37.7	-38.6, -35.8	12.1
	15	305.80	-0.24	-25.4	-44.5, -10.4	1087.8

$$|\mu_{ul}|^2 \;=\; \frac{K^2}{J(J+1)}\,\mu^2 \qquad (6)$$

The column density N_u refers to the upper transition level, we make use of the Boltzmann equation with the assumed T_{ex} to estimate the total column density $N(1,1)$ assuming that both levels are evenly populated:

$$N(1,1) = N_u + N_l = N_u(1 + e^{h\nu/kT_{ex}}) \qquad (7)$$

the metastable inversion transitions, i.e., $J = K$ gives the most reliable estimate of the rotational temperature T_{12}. Using the (1,1) and (2,2) excitation levels, we make use of the rotational temperature equation from Wilson et al. (1993):

$$T_{12} = \frac{41.2}{\ln\left[3.57\,(T_{11}/T_{22})\right]} \qquad (8)$$

where T_{11} and T_{22} is the main beam brightness temperatures of the NH$_3$ (1,1) and (2,2) transition. We do not detect NH$_3$ (2,2) emission in clumps 10, 11 and 15, and therefore we are unable to calculate the rotational temperature for these clumps. However, we are able to calculate a range of values for each parameter of interest such as H$_2$ column and number densities and clump masses, using a range of rotational temperatures typical of similar clumps (10 - 40 K; e.g., Wu et al. 2006, Tieftrunk et al. 1998). This range of temperatures corresponds to at most a factor of two difference in column density and so will not affect our results considerably. In order to obtain H$_2$ column densities we have assumed an ammonia fractional abundance of 3×10^{-8} (Wu et al. 2006; Harju et al. 1993). The H$_2$ densities and clump masses have been calculated using the clump area defined by the Fellwalker algorithm. We have made use of the metastable transitions and this may not resemble a true Boltzmann distribution, nevertheless, T_{12} is a good indicator of the gas temperature T_{kin} for temperatures less than 20 K, although T_{12} underestimates T_{kin} for temperature over 20 K (see e.g. Walmsley & Ungerechts 1983; Danby et al. 1988). We are able to calculate the kinetic temperature using:

$$T_{kin} = T_{12} \times \left(1 + \frac{T_{kin}}{41.5}\right) \times \ln\left(1 + 0.82 \times e^{(-21.45/T_{kin})}\right) \qquad (9)$$

We estimate the total column density of NH$_3$ within the clumps using the following equation assuming that only metastable levels are populated:

$$N(NH_3) = N(1,1)\left(\frac{1}{3}e^{23.4/T_{12}} + 1 + \frac{5}{3}e^{-41.5/T_{12}} + \frac{14}{3}e^{-101.5/T_{12}}\right) \qquad (10)$$

We can test the stability of the cores against collapse by calculating the virial mass, which we derive using the standard equation (e.g., Evans 1999):

$$M_{vir} \simeq 210 R_{core}\langle\,\Delta V^2\,\rangle \qquad (11)$$

where R_{core} is the ammonia clump radius (geometric average dimensions given in Table 2) in parsecs (assuming distance of 4 kpc) and ΔV is the FWHM line width. The resulting parameters for each clump are presented in Table 6.

4 DISCUSSION

4.1 General physical properties of the molecular material

The spatial distribution and morphology of the detected ammonia clumps are given in section 3.1, here we describe the basic parameters. We find NH$_3$ column densities on the order of 10^{14} cm^{-2} the highest values are found closest to the PDR boundary. Unfortunately we are unable to derive the gas density directly from our measurements, as the derivation of the line excitation temperature which is sensitive to density, requires an assumption of the unknown beam filling factor. We find kinetic temperatures between 21 - 31 K with an average of 25 K, this value is above the High (22.4 K) and Low (21.7 K) groups of Molinari et al. (1996) and similar to the values found in a survey of ammonia clumps in the Orion and Cepheus clouds by Harju et al. (1993). An important caveat is that these regions are at different distances to G305 and observed with higher resolution and depth. We assume that our derived column densities are a lower limit due to beam dilution, and the unknown beam filling factor. The NH$_3$ (1,1) and (2,2) emission appears to be biased to cool gas which is extended over the size of the Mopra beam and does not reflect the physical conditions of the unresolved dense cores and filaments we expect to find at sub arc minute scales. The presence of hotter gas is indicated by (3,3) emission and so clumps 1 - 5 and 8 are likely to be more evolved than other, cooler clumps. The clumps that exhibit (3,3) emission are found to correlate well with PAH emission, with the strongest and therefore hottest clumps found close to the central cavity boundary.

Using an assumed NH$_3$ to H$_2$ abundance ratio of 3×10^{-8} we calculate H$_2$ column densities of $> 10^{22}$ cm^{-2}. We assume that the ammonia abundance fraction is constant across the entire region, which is not likely to be the case, however with our current low resolution observations our chosen value gives an appropriate estimate. The abundance ratio of NH$_3$ to H$_2$ has been found to vary from 1×10^{-7} to 1×10^{-8} according to the study of Orion clumps (Harju et al. 1993), thus our measurements of the H$_2$ column density could be an order of magnitude lower than shown in Table 6 and so our results should be taken as an upper limit.

The sizes of the NH$_3$ clumps have been derived using the geometric mean of the linear x and y distances, they range from 2.6 to 10.1 pc. The sizes of the (2,2) emission are smaller than those of the (1,1) emission in all cases and in the same way (3,3) emission is smaller than (2,2) emission. The size of these clumps is significantly greater than those detected in a survey carried out by Wu et al. (2006) (0.4-3.1 pc) and similar observation in the Orion and Cepheus cloud carried out by Harju et al. (1993) (mean 0.3 pc). However the same differing resolution and sensitivity caveat applies, and due to our large beam we are only able to resolve NH$_3$ structure of > 2.6 pc.

We calculate masses for the clumps in excess of a thousand solar masses, with a combined mass of $\sim 6 \times 10^5$ M$_\odot$. It is clear that there is sufficient dense molecular gas to form multiple massive stellar clusters within the detected clumps, and this is likely to occur around the central region. The virial mass is found to be significantly less than the calculated mass for all clumps, we would therefore assume these clumps are gravitationally bound and given the large difference between their actual masses and their virial masses it is likely they are in a state of gravitational collapse, however this may not be an appropriate comparison. The mass of the detected clumps in G305 is higher than expected for isolated clumps that tend to have mass on the order of a few tens to hundreds of solar masses. The simplest explanation for this is that our detected clumps are in fact comprised of a number of unresolved clumps.

Table 6. NH_3 Clump parameters including; main line and integrated optical depth, rotational temperature, kinetic temperature H_2 column density, derived mass and virial mass.

Region	Clump No	$\tau_{(1,1,m)}$	$\int \tau_{(1,1)}$	T_{12} (K)	T_{kin} (K)	$N(H_2)$ $10^{22}cm^{-2}$	Mass $10^3(M_\odot)$	Virial mass $10^3(M_\odot)$
NE	1	0.79	6.5	21.3 ± 0.6	25.2 ± 0.9	6.4 ± 1.8	88 ± 25	31
	3	1.13	11.3	22.3 ± 0.9	26.8 ± 1.5	11.2 ± 4.7	53 ± 22	24
NW	4	1.32	15.8	23.5 ± 1.2	28.8 ± 2.1	15.3 ± 7.4	122 ± 59	51
	7	0.86	5.7	20.1 ± 0.8	23.2 ± 1.2	5.7 ± 2.7	43 ± 20	14
	9	0.29	1.9	19.5 ± 1.1	22.4 ± 1.6	1.9 ± 1.2	5 ± 3	16
SE	2	0.79	8.3	21.1 ± 0.5	24.8 ± 1.2	8.2 ± 3.2	70 ± 27	37
	8	1.03	15.0	24.4 ± 1.6	30.6 ± 2.9	14.6 ± 9.7	69 ± 46	54
	6	0.47	3.5	20.6 ± 0.8	24.0 ± 1.3	3.5 ± 2.3	25 ± 16	17
W	5	1.06	6.8	18.7 ± 0.9	21.2 ± 1.3	6.9 ± 3.8	46 ± 25	11
	10	1.10	8.5	10 - 40	10 - 74	9 - 16	21 - 37	8
	11	1.46	10.2	10 - 40	10 - 74	11 - 20	27 - 48	9
	12	0.36	1.8	18.3 ± 1.2	20.7 ± 1.8	2.0 ± 1.5	3 ± 2	2
	13	1.34	11.7	20.9 ± 1.2	24.6 ± 1.9	11.6 ± 7.3	43 ± 27	14
	14	1.23	10.7	21.2 ± 1.3	25.1 ± 2.1	10.5 ± 7.2	22 ± 15	12
	15	1.51	8.5	10 - 40	10 - 74	9 - 17	11 - 20	4

In previous higher resolution studies of NH_3 clumps Harju et al. (1993) the average size of the clumps is significantly lower than our resolving limit of 2.6 pc, therefore it is no surprise that the average mass of these smaller clumps in the Cepheus, Orion and Taurus clouds are found to be 15 or 140, 15 and 4 $M_\odot$ significantly less than our estimates. Given these average clump masses and sizes and comparing to our derived values it is apparent that the clumps that we have detected in G305 most likely consist of a significant number of unresolved clumps and therefore may be better described as" clouds" rather than "clumps".

As mentioned above we are unable to directly estimate the gas density however we can make estimate of the density of the ammonia clumps by assuming the clumps are spherically symmetric and our estimation of the excitation temperature is correct. This results in a H_2 number density of $\sim 1 \times 10^3 cm^{-3}$ for the largest clumps in the NE, NE and SE region, significantly lower than the critical density of ammonia of $10^4 - 10^5 cm^{-3}$, we find that the smallest clumps detected in the western region have the highest H_2 number densities of $\sim 10^4$. This is further evidence that the large clumps we find in the NE, NW and SE region are in fact comprised of unresolved sub structure which are smoothed by the beam into the single clumps we detect. It appears that the mass of several unresolved clumps is spread out over the detected area by the $\sim 2'$ beam, this drives down the estimated density for the largest clumps but has less of an effect on the smaller clumps which are likely to consist of at most a few cores. This means that the mass we estimate for the largest clumps is most likely an overestimate as the area of emission appears greater than it physically is.

There is compelling evidence of substructure within the detected clumps, this coupled with the unknown abundance ratio, contribute the main sources of error in our calculations. Thus our results should be taken as an upper limit due to the unknown beam filling factor and may be up to an order of magnitude too high due to the unknown abundance ratio.

4.2 Star formation and ammonia clumps towards G305

A key goal of our observations was to study the relationship between the dense molecular gas in G305, as traced by NH_3 and the distribution of known sites of recent or ongoing star formation. To locate areas of ongoing star formation we make use of the Red Source MSX Survey (RMS) (Urquhart et al. 2008; Hoare et al.

2005) and 6.7 GHz methanol masers drawn from Caswell (2009) and the Methanol Multi Beam (MMB) survey (Green et al. 2009), as well as our H_2O maser results. In Figures 5 - 8, we present a panoramic view of the ongoing star formation towards G305.

The RMS survey aims to locate massive young stellar objects (MYSOs), and so highlight regions of recent star formation. Colour selection in the MSX point source catalogue is used to identify objects with colours the same as well known MYSOs. Many objects have very similar colours to the very red MYSOs, this includes UC HII regions, compact planetary nebula, low mass YSOs and evolved stars. We have selected objects that are either MYSOs, YSOs, HII or UC HII detections. We do not distinguish between the different types of selected RMS sources as we will be using them only as a general indicator of recent star formation and have insufficient numbers to carry out any statistical analysis. We find 26 RMS sources in the direction of G305 and overplot these with red boxes in Figures 5 - 8.

The Methanol Multi Beam survey Green et al. (2009) is the widest area survey yet carried out for 6.7 GHz methanol masers, comprising an initial maser search with Parkes and sub-arcsecond positional followup by the Australia Telescope Compact Array and MERLIN. Methanol masers have been recognised as one of the brightest signposts to the formation of massive young stars, (Menten 1991) and unlike other strong masers (OH, H_2O and SiO) have thus far only found close to high mass star forming regions (Minier et al. 2003). The MMB survey has not yet published their catalogue for the l=305 region and so we use preliminary maser positions kindly provided by the MMB team (Fuller & Caswell, priv. comm.) and masers previously documented by Caswell (2009) we identify 13 6.7 GHz methanol masers in the direction of G305 and overplot their locations with cyan circles in Figures 5 – 8. Below we briefly describe the locations of star formation tracers with respect to the ammonia emission.

NW Region: In this region (Fig. 5) we note the highest number of RMS sources (nine) of which six are found within and around the periphery of clump 4. Two RMS sources are seen to the west of clump 7 and one RMS source is seen within clump 9. We find two methanol masers associated with clump 4, one is seen just outside the leading edge of the ammonia emission facing WR48 a, the other methanol maser is seen towards the centre of the clump. Three H_2O masers are detected, two of which reside within clump

Figure 5. NH$_3$ (1,1) and (2,2) emission contoured over greyscale GLIMPSE 5.4 µm image in black and red respectively clump numbers are shown within circles. Detected H$_2$O masers are shown by blue crosses, MMB sources by yellow circles and RMS sources by red boxes. Contours begin at 0.15 K and increment by 0.1 K.

Figure 6. NH$_3$ (1,1) and (2,2) emission contoured over greyscale GLIMPSE 5.4 µm image in black and red respectively, clump numbers are shown within circles. Detected H$_2$O masers are shown by blue crosses, MMB sources by yellow circles and RMS sources by red boxes. Contours begin at 0.15 K and increment by 0.1 K.
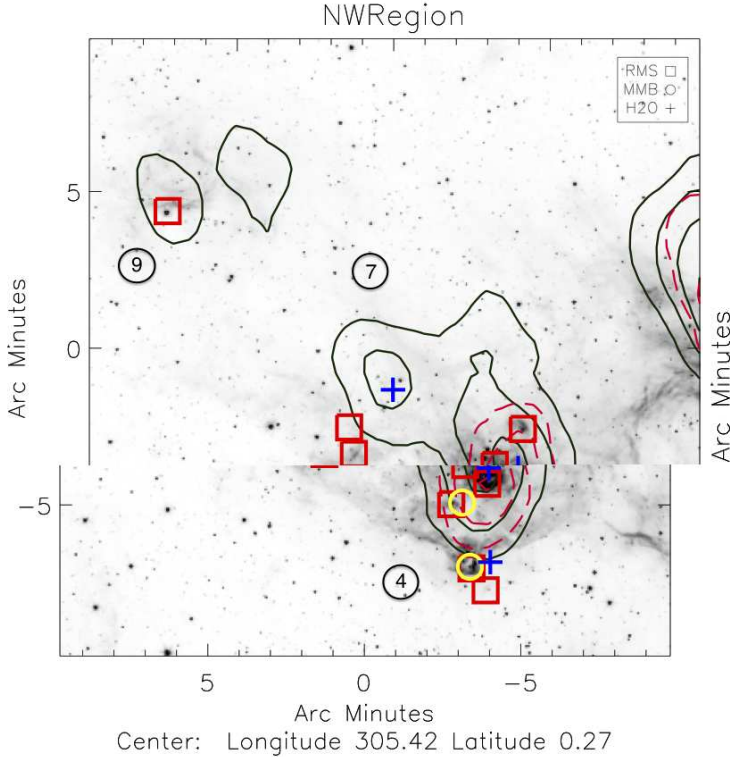
4 and one within clump 7 again close the clump centres. It is interesting that we see RMS sources, H$_2$O masers and methanol masers all within the bounds of clump 4. as mentioned in section 3.1 unlike other regions we see that the clump is coincident with strong PAH emission towards the centre of clump. High resolution observations are required to resolve the internal structure and kinematics but it is likely that there are a number of individual dense cores at different velocities contributing to the large FWHM line width of clump 4. The RMS and MMB sources appear to lie around the core of the detected clumps and are predominantly found on the western side of the clump. The H$_2$O masers again are located close to the clump cores. Nine 1.2 mm cores are detected by Hill et al. (2005) six are found within clump 4, three are found in clump 9. Clump 1 in the NE region is the largest clump in geometric size but clump 4 is the most massive

NE Region: In the bounds of this region (Fig. 6) we find four RMS sources, three of which are found along the western edge of the NH$_3$ emission, one is located close the centre of clump 3. There are three methanol masers, two of which (G305A and B) are found close the centre of clump 3 and one on the western edge of clump 1 coincident with an RMS source and strong PAH emission. The two methanol masers G305A and B are found to be coincident with CH$_3$OH emission, which surrounds the two masers and is elongated to the north. We note the position of a HII region (see Clark & Porter (2004)) to the west of the detected NH$_3$ clumps, seen as a ring in the 5.4 µm PAH emission, this coincides with the low density region separating clump 1 and 3. Star formation tracers are
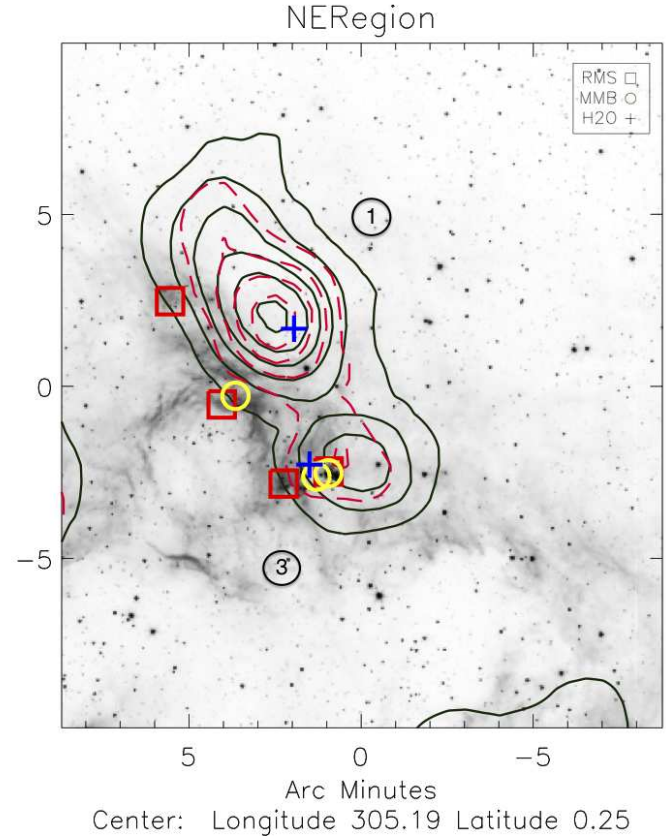
clustered on the western side of the region facing this HII bubble, there are no signs of star formation to the east of the clumps. We detect two H$_2$O masers towards the centre of two clumps. It appears that RMS and MMB star formation tracers are confined within the lower density NH$_3$ facing the ionising HII region to the west, the H$_2$O masers however are found embedded towards the centre of the two clumps.

This region has been studied in some detail (Walsh & Burton 2006; Hill et al. 2005; Longmore et al. 2007). Hill et al. (2005) detect nine 1.2 mm cores within this region concentrated within clump 1 but offset from the peak to the west. Observations in the mid infrared Walsh et al. (2001), near infrared Walsh et al. (1999) and mm line observations Walsh & Burton (2006) (^{13}CO, HCO$^+$, N$_2$H$^+$, CH$_3$CN and CH$_3$OH) were carried out towards the two methanol maser sites designated G305A and G305B (G305.21+0.21 and G305.20+0.21). These methanol masers are shown in Fig. 6 as the most southern two masers, the centre of the detected molecular emission was found to be G305A which has no detected infrared or radio continuum (however we do find it is coincident with a 1.2 mm core). Walsh concludes that G305A is a site of massive star formation similar to the Class 0 stage of low-mass star formation. G305B is coincident with a bright, red infrared source whose bolometric luminosity suggests it should produce a detectable HII region, yet none has been detected. This suggests that G305B may also be at a very early stage of

Figure 7. NH$_3$ (1,1) and (2,2) emission contoured over greyscale GLIMPSE 5.4 μm image in black and red respectively, clump numbers are shown within circles. Detected H$_2$O masers are shown by blue crosses, MMB sources by yellow circles and RMS sources by red boxes. Contours begin at 0.15 K and increment by 0.1 K.

Figure 8. NH$_3$ (1,1) and (2,2) emission contoured over greyscale GLIMPSE 5.4 μm image in black and red respectively, clump numbers are shown within circles. Detected H$_2$O masers are shown by purple circles and RMS sources by red boxes. Contours begin at 0.15 K and increment by 0.1 K.
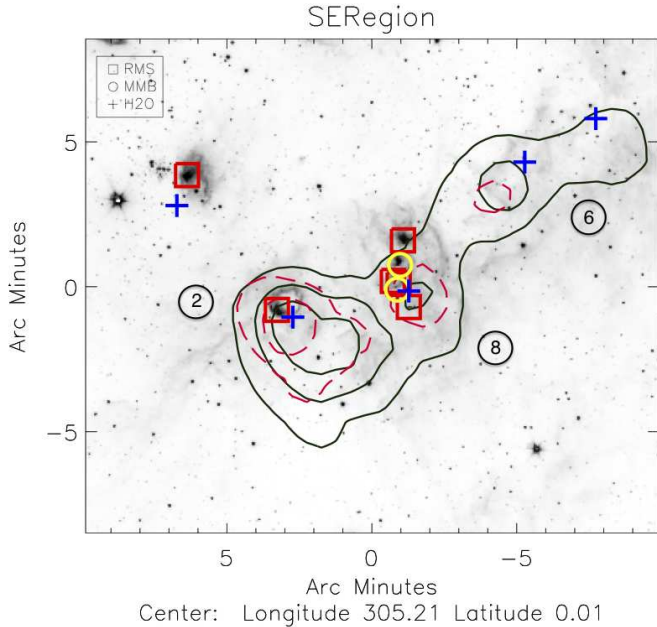
evolution, but probably older than G305A. Longmore detect twelve embedded sources with significant IR excess in this region located around the southern edge of clump 3 within the region of low emission separating clump 1 and 3. An embedded source is found in the centre of the HII region highlighted by 5.4 μm PAH emission to the west of clump 1 and 3. Longmore et al. (2007) conclude that the expanding bubble may be responsible for triggering a third generation of star formation in clump 1 and 3.

SE Region: This region is shown in Fig. 7, coincident with this strip of NH$_3$ emission we find five RMS sources, four H$_2$O masers and two methanol masers. We also note that in the central cavity of G305 there is an RMS source and H$_2$O maser coincident with strong PAH emission but devoid of any NH$_3$ emission. The Four H$_2$O masers within the NH$_3$ emission are all in close proximity to the cores of the NH$_3$ emission. A striking feature of the region is that four of the five RMS sources and both methanol masers are clustered within the low density region of clump 8 and extend towards the core of the clump, this area is also the location of a HII region documented in Clark & Porter (2004), this is clearly a very active area of ongoing star formation. All of these star formation tracers are found on the inward side of the ammonia emission close to the boundary between the central cavity, again facing the ionising central sources. Hill et al. (2005) detect seven 1.2 mm cores, four of these are found in the intense star forming region between clumps 8 and 6.

W Region: This region, shown in Fig. 8 is distinctly different from the other regions we have discussed. We find a total of eight RMS sources, six MMB sources and six H$_2$O masers. Whereas the previous regions all show strong NH$_3$ emission around the periphery of the central HII region, this region shows no significant
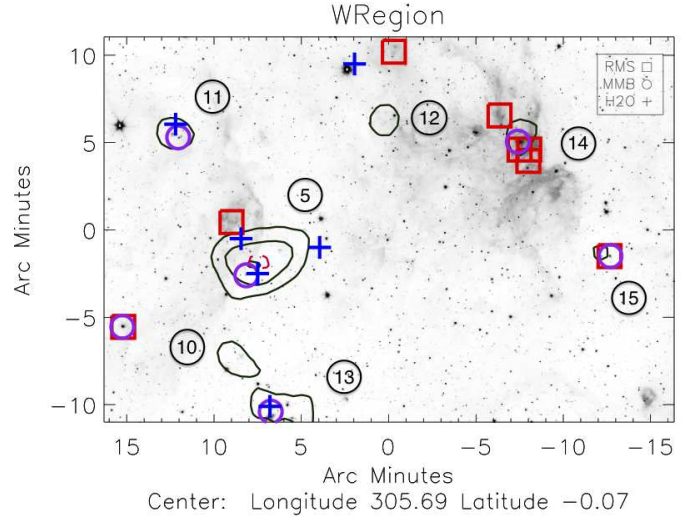
NH$_3$ at this boundary. However, in the absence of any significant ammonia emission at the boundary we do still see significant signs of star formation coincident with clump 14 close to the cavity boundary, with four RMS sources and a single MMB source. Further to the west of the cavity we see dispersed signs of ongoing star formation the majority of which are associated with isolated NH$_3$ emission. Clump 5 is host to three H$_2$O masers, the most detections coincident with a clump in the complex. This region is also host to the most methanol maser detections, 5 of which are found on the edge of NH$_3$ clumps. Hill et al. (2005) detect eleven 1.2 mm cores, which are confined to clump 14 and clump 13. Unlike the other regions where 1.2 mm emission is correlated with strong NH$_3$ (1,1) and (2,2) emission, there is no 1.2 mm emission associated with the strongest ammonia emission in this region, in clump 5. It is clear that this region is host to star formation, however there is much less molecular material in this region and the star formation appears much more dispersed.

It is clear that all regions are host to significant signs of ongoing star formation. Of all the detected clumps only clump 1 and 3 have been studied in any detail by the authors (mentioned in the NE clump section). A striking feature of all these signs of star formation is that they are for the most part all coincident with dense molecular material and are located only on the side of the molecular emission facing the PDR. In cases where we appear have a side on line of site we see star formation only occurring in the low density regions of the ammonia clumps with exception to H$_2$O masers, which appear closer to the dense clump cores. This is most apparent in the NE and S regions, where RMS and MMB detections are seen only in the less dense gas towards the PDR, whereas H$_2$O masers are found deeply embedded in the NH$_3$ emission. This may indicate an age spread in the star formation with H$_2$O masers highlighting a younger age of star formation embedded towards the dense clump centres and older YSOs and visible HII regions found on the clump periphery in the lower density regions. Warmer clumps, highlighted by NH$_3$ (3,3) emission, correlate well with regions of intense star

Table 7. G305 Comparison, column 3 is molecular mass and column 5 shows the number of massive OB stars in the complex. Parameters have been taken from a literature search, numbers in brackets correspond to the following papers.

Region	Distance	Mass	NLyc	Stars
	kpc	$M_\odot$	10^{49} s^{-1}	OB
G305	3.5 - 4 (1)	10^5 (*)	145.5 (2)	> 31 (1)
W49A	10.2 - 12.6 (4)	10^6 (3)	171.7 (2)	> 40 (4)
NGC3603	5 - 8 (5)	10^5 (5)	187.7 (2)	20 (6)
M17	1.3 - 1.9 (9)	10^4 (9)	53.7 (2)	16 (9)
W3 main	1.9 - 2.1 (10)	10^4 (10)	8.8 (2)	12 (10)
Rosette Nebula	1.4 - 1.6 (11)	10^5 (11)	9.8 (14)	30 (11)
Westerlund 2	5 - 7 (12)	10^5 (12)	95.9 (2)	> 12 (12)
Carina	2.3 (13)	10^5 (13)	21.6 (2)	65 (13)

(*) This work (1) Clark & Porter (2004) (2) Smith et al. (1978) (3) Smith et al. (2009) (4) de Pree et al. (1997) (5) Nürnberger et al. (2002) (6) Moffat (1983) (7) Dougherty et al. (2009) (8) Luna et al. (2009) (9) Povich et al. (2009) (10) Tieftrunk et al. (1998) (11) Wang et al. (2008) (12) Dame (2007) (13) Smith & Brooks (2008) (14) Churchwell (1975)

formation, indeed all clumps with (3,3) detections are either host to a large number of star formation tracers or strong PAH emission.

In terms of the star formation distributed within G305 and its relation to the dense molecular material surrounding the central cavity, we have expanded on the work of Clark & Porter (2004), who suggested that the morphology of the nebula is strongly suggestive of star formation on the periphery of the cavities (see Clark & Porter 2004 Section 4.3). We confirm that star formation is taking place on the periphery of the central cavity created by Danks 1 & 2, WR48 and also that a potentially younger generation of star formation is taking place around the younger HII regions located around the central cavity, indicating multiple epochs of massive star formation in G305. The dense molecular material surrounding Danks 1 & 2 takes the form of several discrete and massive clumps, with significant "gaps" (particularly towards the western region) highlighting areas where the ionising photons from these massive stellar clusters can escape. Thus the integrated radio flux very likely underestimates the true ionising photon flux from G305. We are still unable to ascertain if the photoionisation driven shocks are responsible for triggering the observed star formation, however we do note a possible age spread in star formation tracers in the regions closest to the cavity. The western region may be more likely to be spontaneous in nature star formation due to its dispersed morphology.

4.3 Comparison

To put G305 into context it is useful to compare the region to other well known GMCs and HII regions in the galaxy. We have performed a literature search and present parameters for comparison in Table 7. It is apparent that G305 is one of the closest and most massive GMCs in the galaxy, with a molecular mass approximately equal to or exceeding that of other well studied regions. G305 is significantly closer than the regions with similar masses detailed in Table 7, and regions that are found closer to the sun tend to have a lower molecular mass. With its numerous HII regions, the integrated Lyc photon count is on par with the most luminous HII regions in the galaxy. However, whereas many of these regions comprise single HII regions, G305 is host to a number of individual HII regions surrounding a central cavity. As proposed in Clark & Porter (2004) given the morphology of the G305 complex and in particu-

lar the fact that sufficient natal material has been dispersed to allow Danks 1 and 2 to become optically visible, there is a likelihood of substantial photon leakage and thus the massive stellar population of G305 is likely to be an underestimate. This would make G305 one of the closest examples of intense massive star formation in the galaxy, comparable to W49A which lies at $\sim 3 - 4$ times the distance.

4.4 Summary

We present radio observations of the $\sim 1.5° \times 1°$ region G305 in order to uncover the dense molecular component of the region. This study includes observations of the NH₃ (1,1), (2,2) and (3,3) spectral lines, as well as the 22 GHz H₂O maser line. To complement our observations we have made use of mid-IR data from the GLIMPSE survey and traced signs of star formation using the RMS and MMB surveys. Combining these data sets has allowed us to obtain a panoramic view of ongoing star formation within G305 and its relation to the dense molecular material.

We detect 15 NH₃ (1,1) clumps, 12 NH₃ (2,2), 7 NH₃ (3,3) clumps and 16 H₂O masers. Our observations reveal that G305 is comprised of several massive molecular clumps mostly found towards the northern and southern edges of the main cavity. The molecular material towards the western region of G305 is more dispersed in nature. Kinetic temperatures of the clumps ranges from $\sim 21 - 31$ K, the total mass of dense gas traced by NH₃ is estimated to be $\sim 6 \times 10^5$ M$_\odot$ with an average clump mass of $\sim 4 \times 10^4$ M$_\odot$. We detect the majority (~80%) of this material in close proximity to the PDR surrounding the central cavity. It is clear that there is sufficient material to form a number of massive clusters and that there is a high degree of interaction between the massive stars and the molecular material. It is possible that such interactions could be responsible for triggering the star formation seen around the periphery of the NH₃ clumps.

We find 27 RMS sources and 13 MMB masers, as well as 16 H₂O masers. With 56 star formation tracers G305 is obviously a region of intense star formation. We are able to clearly identify the PDR and find it correlates with the molecular gas traced by NH₃Ṡtar formation appears to be taking place within and on the periphery of the detected NH₃ clumps, with > 80% of star formation tracers found to be associated with NH₃ emission. In almost all cases star formation is located on the side of the NH₃ clump that faces the ionising radiation highlighted by the PDR, evidence perhaps of triggered star formation.

These low resolution observations are intended as a pathfinder for future high resolution follow up, which will allow us to uncover the sub parsec structure of the ammonia emission we predict is present, and thus allow us to comment on the effects massive star formation is having upon the dense molecular material.

of the NASA/ IPAC Infrared Science Archive, which is operated by the Jet Propulsion Laboratory, California Institute of Technology, under contract with the National Aeronautics and Space Administration.

REFERENCES

Benjamin R. A., Churchwell E., Babler B. L., Bania T. M., Clemens D. P., Cohen M., Dickey J. M., Indebetouw R., Jackson J. M., Kobulnicky H. A., Lazarian A., Marston A. P., Mathis J. S., Meade M. R., Seager S., Stolovy S. R., Watson C., Whitney, B. A., Wolff, M. J., Wolfire, M. G., 2003, PASP, 115, 953

Berry D. S., Reinhold K., Jenness T., Economou F., 2007, in R. A. Shaw, F. Hill, & D. J. Bell ed., Astronomical Data Analysis Software and Systems XVI Vol. 376 of Astronomical Society of the Pacific Conference Series, CUPID: A Clump Identification and Analysis Package. pp 425–+

Breen S. L., Ellingsen S. P., Johnston-Hollitt M., Wotherspoon S., Bains I., Burton M. G., Cunningham M., Lo N., Senkbeil C. E., Wong T., 2007, MNRAS, 377, 491

Caswell J. L., 2009, Publications of the Astronomical Society of Australia, 26, 454

Churchwell E., 1975, in T. L. Wilson & D. Downes ed., H II regions and related topics Vol. 42 of Lecture Notes in Physics, Berlin Springer Verlag, Evolved H II regions. pp 245–+

Churchwell E., Babler B. L., Meade M. R., Whitney B. A., Benjamin R., Indebetouw R., Cyganowski C., Robitaille T. P., Povich M., Watson C., Bracker S., 2009, pasp, 121, 213

Clark J. S., Porter J. M., 2004, aap, 427, 839

Dame T. M., 2007, ApJl, 665, L163

Danby G., Flower D. R., Valiron P., Schilke P., Walmsley C. M., 1988, MNRAS, 235, 229

de Pree C. G., Mehringer D. M., Goss W. M., 1997, ApJ, 482, 307

Dougherty S. M., Clark J. S., Negueruela I., Johnson T., Chapman J. M., 2009, ArXiv e-prints

Elmegreen B. G., 2002, in Geisler D. P., Grebel E. K., Minniti D., eds, Extragalactic Star Clusters Vol. 207 of IAU Symposium, Triggering the Formation of Young Clusters. pp 390–+

Elmegreen B. G., Lada C. J., 1977, ApJ, 214, 725

Furuya R. S., 2003, in J. M. De Buizer & N. S. van der Bliek ed., Galactic Star Formation Across the Stellar Mass Spectrum Vol. 287 of Astronomical Society of the Pacific Conference Series, H_2O Masers in Young Stellar Objects. pp 367–372

Green J. A., Caswell J. L., Fuller G. A., Avison A., Breen S. L., Brooks K., Burton M. G., Chrysostomou A., Cox J., Diamond P. J., Ellingsen S. P., Gray M. D., Hoare M. G., Masheder M. R. W., McClure-Griffiths N. M., Quinn L., Thompson M. A., 2009, MNRAS, 392, 783

Habing H. J., Israel F. P., 1979, araa, 17, 345

Harju J., Walmsley C. M., Wouterloot J. G. A., 1993, aaps, 98, 51

Hill T., Burton M. G., Minier V., Thompson M. A., Walsh A. J., Hunt-Cunningham M., Garay G., 2005, MNRAS, 363, 405

Ho P. T. P., Townes C. H., 1983, araa, 21, 239

Hoare M. G., Lumsden S. L., Oudmaijer R. D., Urquhart J. S., Busfield A. L., Sheret T. L., Clarke A. J., Moore T. J. T., Allsopp J., Burton M. G., Purcell C. R., Jiang Z., Wang M., 2005, in R. Cesaroni, M. Felli, E. Churchwell, & M. Walmsley ed., Massive Star Birth: A Crossroads of Astrophysics Vol. 227 of IAU Symposium, The RMS survey: Massive young stars throughout the galaxy. pp 370–375

Leger A., Puget J. L., 1984, aap, 137, L5

Longmore S. N., Maercker M., Ramstedt S., Burton M. G., 2007, MNRAS, 380, 1497

Luna A., Mayya Y. D., Carrasco L., Rodríguez-Merino L. H., Bronfman L., 2009, in Revista Mexicana de Astronomia y Astrofisica Conference Series Vol. 37 of Revista Mexicana de Astronomia y Astrofisica Conference Series, The large scale molecular environment towards Westerlund 1. pp 32–37

Menten K., 1991, in A. D. Haschick & P. T. P. Ho ed., Atoms, Ions and Molecules: New Results in Spectral Line Astrophysics Vol. 16 of Astronomical Society of the Pacific Conference Series, Methanol Masers and Submillimeter WavelengthWater Masers in Star-Forming Regions. pp 119–+

Minier V., Ellingsen S. P., Norris R. P., Booth R. S., 2003, aap, 403, 1095

Moffat A. F. J., 1983, aap, 124, 273

Molinari S., Brand J., Cesaroni R., Palla F., 1996, aap, 308, 573

Nürnberger D. E. A., Bronfman L., Yorke H. W., Zinnecker H., 2002, aap, 394, 253

Pineda, J. E., Rosolowsky, E. W., & Goodman, A. A., 2009, ApJl, 699, L134

Povich M. S., Churchwell E., Bieging J. H., Kang M., Whitney B. A., Brogan C. L., Kulesa C. A., Cohen M., Babler B. L., Indebetouw R., Meade M. R., Robitaille T. P., 2009, ApJ, 696, 1278

Purcell C. R., 2006, PhD thesis, The University of New South Wales

Smith L. F., Biermann P., Mezger P. G., 1978, aap, 66, 65

Smith N., Brooks K. J., 2008, The Carina Nebula: A Laboratory for Feedback and Triggered Star Formation. pp 138–+

Smith N., Whitney B. A., Conti P. S., de Pree C. G., Jackson J. M., 2009, MNRAS, 399, 952

Tieftrunk A. R., Megeath S. T., Wilson T. L., Rayner J. T., 1998, aap, 336, 991

Urquhart J. S., Hoare M. G., Lumsden S. L., Oudmaijer R. D., Moore T. J. T., 2008, in H. Beuther, H. Linz, & T. Henning ed., Massive Star Formation: Observations Confront Theory Vol. 387 of Astronomical Society of the Pacific Conference Series, The RMS Survey: A Galaxy-wide Sample of Massive Young Stellar Objects. pp 381–+

Urquhart J. S., White G. J., Pilbratt G. L., Fridlund C. V. M., 2003, aap, 409, 193

Urquhart J. S., Hoare M. G., Purcell C. R., Brooks K. J., Voronkov M. A., Indermuehle B. T., Burton M. G., Tothill N. F. H., Edwards P. G., 2010, ArXiv e-prints

Walmsley C. M., Ungerechts H., 1983, aap, 122, 164

Walsh A. J., Bertoldi F., Burton M. G., Nikola T., 2001, MNRAS, 326, 36

Walsh A. J., Burton M. G., 2006, MNRAS, 365, 321

Walsh A. J., Burton M. G., Hyland A. R., Robinson G., 1999, MNRAS, 309, 905

Walsh A. J., Lo N., Burton M. G., White G. L., Purcell C. R., Longmore S. N., Phillips C. J., Brooks K. J., 2008, Publications of the Astronomical Society of Australia, 25, 105

Wang J., Townsley L. K., Feigelson E. D., Broos P. S., Getman K. V., Román-Zúñiga C. G., Lada E., 2008, ApJ, 675, 464

Wilson T. L., Gaume R. A., Johnston K. J., 1993, ApJ, 402, 230

Wu Y., Zhang Q., Yu W., Miller M., Mao R., Sun K., Wang Y., 2006, aap, 450, 607